

Artificial Gauge Field and Quantum Spin Hall States in a Conventional Two-dimensional Electron Gas

Likun Shi¹, Wenkai Lou¹, F. Cheng¹, Y. L. Zou¹, Wen Yang² and Kai Chang¹

¹*SKLSM, Institute of Semiconductors, Chinese Academy of Sciences, P.O. Box 912, Beijing 100083, China and*

²*Beijing Computational Science Research Center, Beijing 100094, China*

Based on the Born-Oppenheimer approximation, we divide total electron Hamiltonian in a spin-orbit coupled system into slow orbital motion and fast interband transition process. We find that the fast motion induces a gauge field on slow orbital motion, perpendicular to electron momentum, inducing a topological phase. From this general designing principle, we present a theory for generating artificial gauge field and topological phase in a conventional two-dimensional electron gas embedded in parabolically graded GaAs/In_xGa_{1-x}As/GaAs quantum wells with antidot lattices. By tuning the etching depth and period of antidot lattices, the band folding caused by superimposed potential leads to formation of minibands and band inversions between the neighboring subbands. The intersubband spin-orbit interaction opens considerably large nontrivial minigaps and leads to many pairs of helical edge states in these gaps.

PACS numbers: 71.70.Ej, 75.76.+j, 72.25.Mk

I. INTRODUCTION

Exploring of various topological quantum states is always one of the central issue of condensed matter physics [1–3]. Topological insulators (TIs) [4], a new class of solids, possess unique properties such as robust gapless helical edge or surface states and exotic topological excitations [4–27]. The helical edge states of two-dimensional (2D) TIs are protected strictly against elastic backscattering from nonmagnetic impurities. This feature leads to dissipationless conducting channels and therefore is promising for possible applications in spintronics, quantum information, thermoelectric transport and on-chip interconnection in integrated circuit. These novel applications require large nontrivial gaps, which suppress the coupling between the edge and bulk states, leading to dissipationless edge transport. For this purpose, there is an ongoing search for feasible realizations of various narrow gap materials containing heavy elements, e.g., CdTe/HgTe/CdTe quantum wells (QWs) [7–9], and Tin film [22]. However, fabrication of high-quality samples of these proposed structures still remains a challenging task, requiring precise control for material growth.

In this work, we demonstrate that conventional semiconductor GaAs/In_xGa_{1-x}As/GaAs two-dimensional electron gas (2DEG) with antidot lattices can be driven into the TI phase. The 2DEGs provide a promising playground for realizing TI states with quite large nontrivial gap (~ 20 meV) operating at liquid nitrogen temperature regime, instead of searching new materials containing heavy atoms. We first present a general analysis for generating an artificial gauge field in a semiconductor 2DEG, then we demonstrate band inversion between neighboring subbands utilizing antidot lattices created by well-developed semiconductor etching technique, and generate the TI phase with many pairs of helical edge states. This suggests a completely new method to generate topological phase in conventional semiconductor

2DEGs without strong spin-orbit interaction (SOI), at liquid nitrogen temperature regime.

II. GAUGE FIELD FROM BORN-OPPENHEIMER APPROXIMATION

First we discuss the emergence of an artificial gauge field in a system of electrons in a 2D system described by a low-energy single-particle Hamiltonian $H = \epsilon(\mathbf{k})\sigma_0 \otimes \tau_0 + \sum_{i,j=1}^3 d_{ij}(\mathbf{k})\sigma_i \otimes \tau_j$, where σ_i and τ_i ($i = 1, 2, 3$) are Pauli matrices describing the electron spin and the conduction ($\tau_3 = +1$) and valence ($\tau_3 = -1$) bands, respectively, and $\sigma_0 = \tau_0 = I_{2 \times 2}$ are identity matrices. Taking $d_{31} = Ak_x$, $d_{02} = Ak_y$, $d_{03} = M - Bk^2$ and other $d_{ij} = 0$, we obtain the Bernevig-Hughes-Zhang (BHZ) Hamiltonian for 2D TIs [7]. Neglecting the band index τ , and taking $d_1 = -\alpha k_y - \beta k_x$, $d_2 = \alpha k_x + \beta k_y$, $d_3 = 0$, we get the Hamiltonian for a 2DEG with Rashba and Dresselhaus SOIs, where α and β are the strengths of Rashba and Dresselhaus SOIs, respectively. Next, we divide the total Hamiltonian into the intra-band, slow part $H_{\text{orb}} = \epsilon(\mathbf{k})\sigma_0 \otimes \tau_0$ and the inter-band, fast part $H_{\text{IB}} = \sum_{i,j=1}^3 d_{ij}(\mathbf{k})\sigma_i \otimes \tau_j$, which usually arises from the SOIs in real materials. The eigenstate of the total Hamiltonian can be decomposed into the fast and slow components: $|\Psi(\mathbf{k})\rangle = \sum_n \phi_n(\mathbf{k})|\chi_n(\mathbf{k})\rangle$, where $\{|\chi_n(\mathbf{k})\rangle\}$ are eigenstates of the fast part H_{IB} and $\{\phi_n(\mathbf{k})\}$ describe the slow part. The fast spin dynamics compared with the slow orbital motion allow us to make the Born-Oppenheimer approximation, i.e., neglecting the coupling between different $|\chi_n(\mathbf{k})\rangle$, and derive an effective Hamiltonian governing the slow orbital motion $\phi_n(\mathbf{k})$ (see Appendix A):

$$\begin{aligned} H_n(\mathbf{k}) &= \langle \chi_n(\mathbf{k}) | H_{\text{orb}}(\mathbf{k}, \hat{\mathbf{r}}) + H_{\text{IB}}(\mathbf{k}, \hat{\sigma}) | \chi_n(\mathbf{k}) \rangle \\ &= H_{\text{orb}}(\mathbf{k}, \hat{\mathbf{r}} - \mathbf{A}_n) + \epsilon_n(\mathbf{k}), \end{aligned} \quad (1)$$

where $\epsilon_n(\mathbf{k}) = \langle \chi_n(\mathbf{k}) | H_{IB} | \chi_n(\mathbf{k}) \rangle$ acts as an effective potential that separates different bands $\{|\chi_n(\mathbf{k})\rangle\}$ and $\mathbf{A}_n = -i \langle \chi_n(\mathbf{k}) | \partial_{\mathbf{k}} | \chi_n(\mathbf{k}) \rangle$ is a gauge potential in the momentum space of the slow orbital motion, due to the interband coupling to the fast spin dynamics [28, 29]. For the BHZ Hamiltonian, the gauge potential \mathbf{A}_n leads to an effective Lorentz force $F_{xy,n}(\mathbf{k})$ in the momentum space perpendicular to the electric field \mathbf{E} :

$$F_{xy,n}(\mathbf{k}) \equiv i[x', y'] = i[i\partial_{k_x} - A_{x,n}, i\partial_{k_y} - A_{y,n}] \\ = s_n t_n \frac{A^2(M + Bk^2)}{2[A^2k^2 + (M - Bk^2)^2]^{3/2}}, \quad (2)$$

where $s_n = \pm 1$ denotes spin up or down state while $t_n = \pm 1$ denotes the conduction or valence band, respectively ($n = 1, 2, 3, 4$). The Chern number $C_n = (1/2\pi) \int_{BZ} d^2k F_{xy,n} = s_n t_n [1 + \text{sign}(M/B)]/2$ is obtained by integrating the field strength $F_{xy,n}$ in the Brillouin zone. The sign change in M would induce a change of the Chern number by 1, which corresponds to the topological phase transition [30, 31].

For a 2DEG with Rashba and Dresselhaus SOIs, we find $F_{xy}(\mathbf{k}) = 0$, which means that the Chern number vanishes in 2DEG with SOIs. Comparing the Hamiltonian of 2D TIs to that of 2DEGs with SOIs, one can see clearly that 2D TIs possess an additional degree of freedom: the band index τ . In order to generate the gauge field and realize TI phases in a 2DEG, one needs to create minibands and band inversion in 2DEGs.

III. EFFECTIVE HAMILTONIAN AND QUANTUM SPIN HALL STATES

Based on the above designing principle, we will create topological phase in conventional semiconductor 2DEG. This is the first demonstration of the formation of a TI phase in the *s-like* band systems, i.e., a 2DEG with nanostructured antidot lattice shown schematically in Fig. 1(a). Nanostructured antidot lattices, consisting of periodically arranged holes that are etched in a 2DEG, form a strongly repulsive egg-carton-like periodic potential in a 2DEG [32–39]. This artificial crystals lead to a wide variety of phenomena, for instance, Weiss oscillation, chaotic dynamics of electrons, the formation of an electronic miniband structure and massless Dirac fermions. At low temperatures, the mean free path of electrons is much longer than the period of antidot lattices ranging from 10 to 100 nanometers. The modulated periodic potential can also be created by electron beam lithography electrodeposition and periodic arrays of metallic nanodots can be realized on semiconductor surfaces. Due to elastic strains producing these dots, a sufficiently strong piezoelectric potential modulation results in miniband effects in the underlying 2DEG [34, 35]. Very recently, a honeycomb lattice of coronene molecules was created by using a cryogenic scanning tunneling microscope on a Cu(111) surface to construct artificial

graphene-like lattice with the lattice constant approaching 5nm [39].

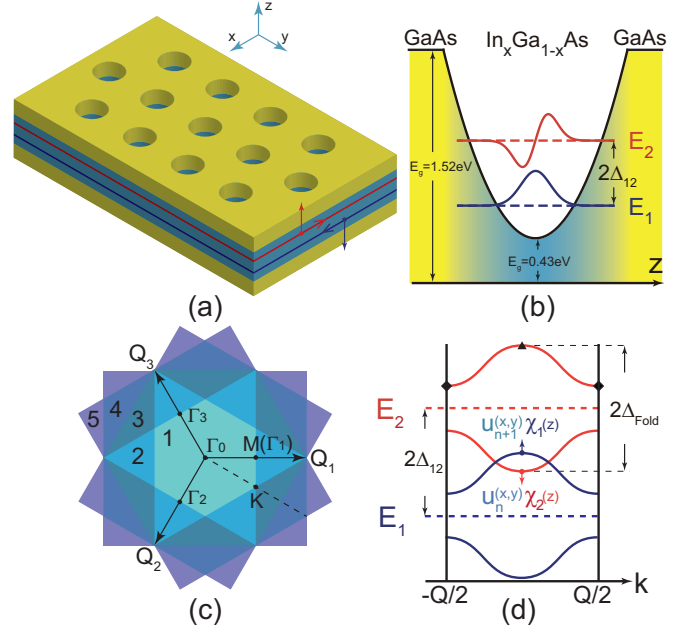


FIG. 1: (color online) Schematic of the proposed structure and its energy bands. (a) A GaAs/ $\text{In}_x\text{Ga}_{1-x}\text{As}$ /GaAs parabolically graded QW with an antidot lattice, which can be created by etching technique. (b) Band profile and the first and second subbands of the parabolically graded QW. (c) Brillouin zone folding induced by a triangular antidot lattice. The numbers 1 – 5 denote the first to the fifth Brillouin zones of the antidot lattice. (d) Minibands of the antidot lattice from folding the first and second subbands of the QW ($Q = 2\pi/a$ and a is the antidot lattice constant). Note that band inversion occurs between neighboring minibands.

We consider the 2DEG in a GaAs/ $\text{In}_x\text{Ga}_{1-x}\text{As}$ /GaAs PQW, which was fabricated successfully before [40–42], with a triangular antidot lattice (see Fig. 1(a)). Before going to the numerical calculation, we first give a clear physical picture for the emergence of a TI phase in this 2DEG system upon nanostructuring with antidot lattice. The simplest description of the 2DEG system is obtained by reducing the eight-band Kane model to the lowest conduction subbands of the QW (see Appendix B). This gives the Hamiltonian for the 2DEG with periodic antidot lattice potential $V(x, y)$:

$$H = \hbar^2 k^2 / 2m + \Delta_{12} \tau_z + \eta \tau_x (k_x \sigma^x + k_y \sigma^y) + V(x, y), \quad (3)$$

where τ_i ($i = x, y, z$) are Pauli matrices describing the first and second QW subbands $\{|\chi_n(z)\rangle\}$ ($n = 1, 2$) of effective mass m , and σ^i ($i = x, y, z$) refer to the electron spin. The second term $\Delta_{12} \tau_z$ comes from the energy difference $2\Delta_{12}$ between the first and second subbands [see Fig. 1(b)]. The third term $\eta \tau_x (k_x \sigma^x + k_y \sigma^y)$ describes the inter-subbands SOI (ISOI) obtained from the eight-band Kane model using the Löwdin perturbation theory

(see Appendix B). The coupling strength η is

$$\eta = \frac{1}{3} \langle \chi_2(z) | \sum_{i=g,g'} \left(P^2(z) \frac{\partial_z E_i(z)}{E_i^2(z)} + P(z) \frac{\partial_z P(z)}{E_i(z)} \right) | \chi_1(z) \rangle, \quad (4)$$

where $E_g(z)$ and $\Delta_0(z)$ are the band gap and spin split-off splitting in the QW region, $E_{g'}(z) \equiv E_g(z) + \Delta_0(z)$, and $P(z)$ is the Kane matrix element. The SOIs in 2DEGs usually come from the asymmetry of the QWs, i.e., Rashba SOI. Surprisingly, the ISOI can appear in a symmetric PQW, behaving like a hidden SOI. From Eq. (4), one can see that the ISOI arises from the spatial variations of the bandgap $E_g(z)$, the Kane matrix $P(z)$, and the intrinsic SOI $\Delta_0(z)$, i.e., the variation of the concentration of *In* component, which behaves like an effective local electric field. This local electric field would not push the electron and the hole states to the left and right sides of the QW, but it can induce a considerably large ISOI hidden in symmetric QWs. The initial $|\chi_1(z)\rangle$ and final states $|\chi_2(z)\rangle$ are neighboring subbands having opposite parity, while the variations of $E_g(z)$, $P(z)$ and $\Delta_0(z)$ in a symmetric QW are odd. This means that the ISOI can exist in symmetric QWs.

The first and second subbands both form minibands due to the Brillouin zone folding caused by the antidot lattice. The band inversion could occur between the two adjacent minibands of the first subband $\psi_+ = \chi_1(z)u_{k,n_1}(x,y)$ and the second subband $\psi_- = \chi_2(z)u_{k,n_2}(x,y)$ (see Fig. 1(d)), where $u_{k,n}(x,y)$ is the n th miniband formed by the antidot lattice. We model the triangular antidot lattice potential $V(x,y)$ by a periodic potential $V_0[1 + \sum_{i=1}^3 \cos(\mathbf{Q}_i \cdot \mathbf{r})]$ with potential height V_0 , $\mathbf{Q}_1 = (2\pi/a)(1,0)$, $\mathbf{Q}_2 = (2\pi/a)(-1/2, -\sqrt{3}/2)$, $\mathbf{Q}_3 = (2\pi/a)(-1/2, \sqrt{3}/2)$ and a is the triangular antidot lattice constant (see Appendix C).

To describe the four minibands (two spin-degenerate minibands) $|\psi_+, \uparrow\rangle$, $|\psi_-, \downarrow\rangle$, $|\psi_+, \downarrow\rangle$, $|\psi_-, \uparrow\rangle$ involved in the band inversion, we treat other electron and hole minibands by Löwdin perturbation theory and reduce the eight-band Kane $\mathbf{k}\cdot\mathbf{p}$ model to the following effective Hamiltonian within the basis $(|\psi_+, \uparrow\rangle, |\psi_-, \downarrow\rangle, |\psi_+, \downarrow\rangle, |\psi_-, \uparrow\rangle)$:

$$H_{\text{eff}}^{4 \times 4} = \begin{pmatrix} M - Bk^2 & Ak_- & 0 & 0 \\ Ak_+ & -M + Bk^2 & 0 & 0 \\ 0 & 0 & M - Bk^2 & Ak_+ \\ 0 & 0 & Ak_- & -M + Bk^2 \end{pmatrix} \quad (5)$$

(see Appendix D and E), which assumes the same form as the $D = 0$ BHZ Hamiltonian. Here $k_{\pm} = k_x \pm ik_y$, $M = \Delta_{12} - \Delta_{\text{Fold}}$ [see Fig. 1(b)], $B = -\hbar^2/2m^*$, and A characterize the ISOI strength between neighboring minibands with opposite spin. This Hamiltonian obviously has a Z_2 topological phase when $M < 0$, corresponding to band inversion.

Next we employ the eight-band Kane $\mathbf{k}\cdot\mathbf{p}$ model to calculate the subband structure with SOIs in a 40-nm-thick

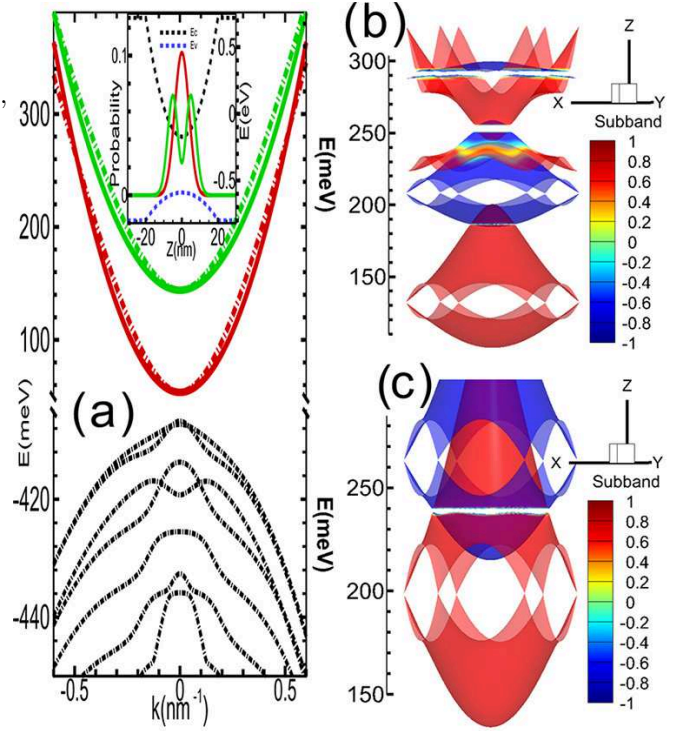


FIG. 2: (color online) (a) Band structure of a GaAs/In_xGa_{1-x}As/GaAs parabolically graded QW from eight-band Kane model. The red and blue dashed (solid) curves denote the first and second subbands from the eight-band Kane model (the reduced four-band model). The inset shows the spatial distributions of the first and second subbands. (b) and (c): minibands of a parabolically graded QW for two different triangular antidot lattices: the lattice constants and barrier heights V_0 of the antidot lattices are $a = 17$ nm, $V_0 = 200$ meV for (b) and 12.5 nm, 300 meV for (c). The minibands are inverted and the minigaps are opened.

GaAs/In_xGa_{1-x}As/GaAs PQWs [40, 41], as plotted in Fig. 2(a). The energy difference between the minima of the first and second subbands at Γ point is about 90 meV [see Fig. 2(a)]. In order to calculate the miniband structures caused by an in-plane periodic potential induced by the triangular antidot lattice, we reduce the eight-band model to an effective four-band $\mathbf{k}\cdot\mathbf{p}$ Hamiltonian by including the lowest 20 electron subbands and 54 highest 'hole' subbands in the QW, to reproduce the energy dispersions of the first and second subbands calculated from the eight-band Kane model [see Fig. 2(a)]. The parameters in the four-band Hamiltonian is given in Appendix E. The minibands from the four-band $\mathbf{k}\cdot\mathbf{p}$ Hamiltonian are shown in Figs. 2(b) and 2(c). These minibands originate from folding the first and second subbands of the QW into the first Brillouin zone of the antidot lattice [Fig. 1(c)]. By tuning the antidot lattice constant a and the potential height V_0 , i.e., the etching depth of the antidot lattice, many band inversions appear between these minibands, which can be clearly seen in Figs. 2(b) and

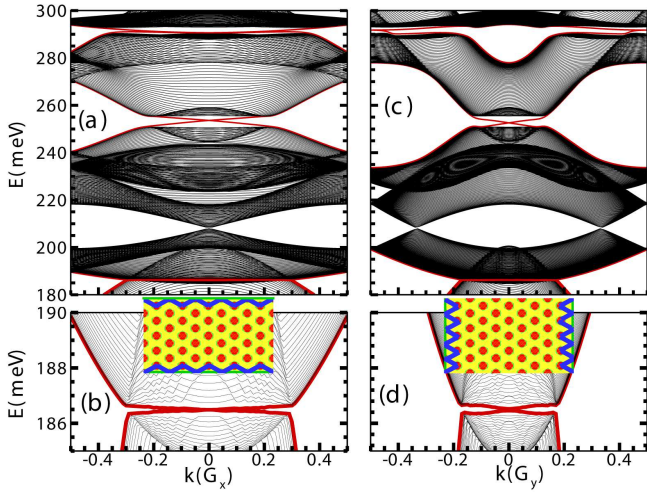


FIG. 3: (color online) Edge states in nontrivial minigaps of a Hall bar structure of the antidot lattice. The Hall bar orientation is along the x axis (a) or y axis (c), as sketched in the insets of (b) and (d), respectively. The lower panels (b) and (d) amplify the lowest nontrivial minigaps and gapless topological edge states. The lattice constant of the antidot lattice is $a = 17$ nm. The blue curves indicate the spatial distributions of the edge states.

2(c). The minigaps between these minibands are opened by the ISOI shown in Eq. (4) [see Figs. 2(b) and 2(c)].

To demonstrate that these minigaps are topologically nontrivial, we determine the parity of each miniband at the four time-reversal invariant momenta [11] Γ_i ($i = 0, 1, 2, 3$) in the first Brillouin zone shown in Fig. 1(c). For the lowest N spin-degenerate minibands being occupied, the Z_2 invariant is given by $(-1)^\nu = \prod_i \delta_i$, $\delta_i = \prod_{m=1}^N \xi_{2m}(\Gamma_i)$, where $\xi_{2m}(\Gamma_i) = \pm 1$ is the parity of the $2m$ th occupied miniband at Γ_i . Our calculation gives $\nu = 1$ at all the minigaps, which proves the whole system is in the quantum spin-Hall phase (see Appendix F).

Next, we demonstrate the emergence of topological edge states upon etching the QW into a Hall bar structure along two different directions (x axis and y axis). As shown in Fig. 3, a pair of topological helical edge states appear inside each nontrivial minigap. For example, we can see topological helical edge states in the lowest two nontrivial minigaps near ~ 186.5 meV and ~ 255 meV, respectively. The helical edge state pairs in these minigaps would lead to higher conductance plateaus as the Fermi energy increases by increasing the doping level. The helical edge states do not overlap with the bulk states, making it possible to be detected experimentally.

The lowest nontrivial minigaps is quite small (about 0.5 meV), but the second minigap is larger (about 5 meV). By tuning the period and potential height of the antidot lattice, the nontrivial minigaps can be significantly enhanced [see Figs. 4(a) and 4(b)]. For example, the lowest minigaps can be enhanced to 5 meV, which is already comparable with that in HgTe and InAs/GaSb

QW systems (~ 10 meV) [8, 9]. The second minigaps can approach 20 meV, which means the TI phase can be realized at liquid nitrogen temperature regime. From Figs. 4(a) and 4(b), one can see that the lowest nontrivial minigap is closed as the lattice constant a increases, but the second higher nontrivial minigap survives, i.e., the TI phase can exist even at large lattice constants, e.g., 25 nm.

Finally, we comment on the experimental detection the aforementioned edge states in GaAs/ $\text{In}_x\text{Ga}_{1-x}\text{As}$ /GaAs quantum Hall bar (shown schematically in the insets of Figs. 3(b) and 3(d)). One way to detect the aforementioned edge states (shown in Fig. 3) is the standard four terminal measurements as demonstrated in previous works [8, 9]. In contrast to HgTe and InAs/GaSb QW systems, there are many pairs of helical edge states in our system between these inverted minibands, which leads to higher plateaus with increasing the Fermi energy. Another possible way is microwave impedance microscopy which makes spatial-resolved nano-scale images (< 100 nm) of the conductivity and permittivity of a sample [43]. The unoccupied edge states in higher minigaps can be detected using the angle-resolved photonemission technique [44], which has already been successfully applied to identify occupied and unoccupied surface states in Bi_2Se_3 and $\text{Bi}_2\text{Te}_x\text{Se}_3$ [44–46].

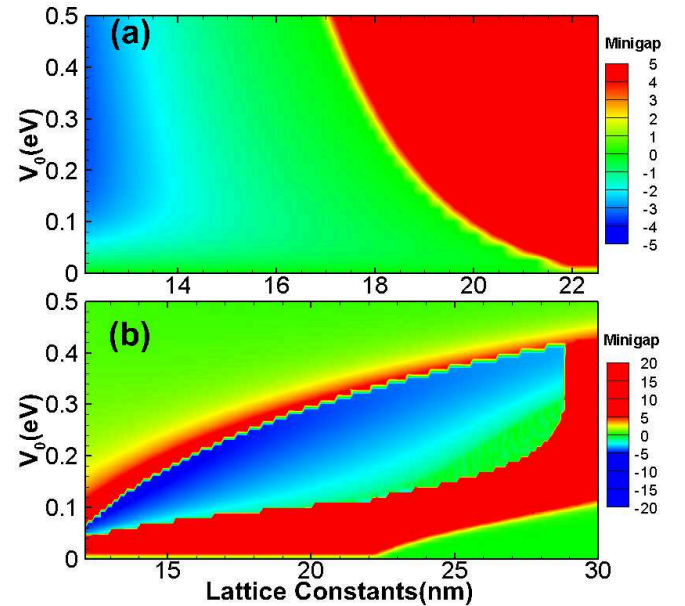


FIG. 4: Phase diagrams of the antidot lattice on a GaAs/ $\text{In}_x\text{Ga}_{1-x}\text{As}$ /GaAs parabolically graded QWs. The lowest (a) and second (b) minigap vs. antidot lattice constant a and potential height V_0 . Negative (Positive) minigap indicates TI phase (normal phase).

IV. CONCLUSION

Our proposal is based on a general analysis about the electron orbital motion in TIs. By using the Born-Oppenheimer approximation, we find that the fast motion will induce a spin-dependent gauge field on slow orbital motion. Based on this general analysis, we demonstrate theoretically the TI phase in a conventional 2DEG embedded in a symmetric GaAs/In_xGa_{1-x}As/GaAs PQW, with antidot lattices created by well-developed etching technique. The key point is to create a ISOI in a symmetric QW, in contrast to conventional SOI in asymmetric QWs. This hidden ISOI in symmetric QWs induces a spin-dependent effective Lorentz force on the electrons, and generates the TI phases in such system. Interestingly, such ISOI exists in conventional semiconductors with a positive bandgap, i.e., normal band structures can generate quite large nontrivial gaps approaching 20 meV. This make it possible to observe the quantum spin Hall effect in liquid nitrogen temperature regime.

So far, all members of TI family are narrow bandgap systems containing heavy atoms. Our proposal breaks this constraint, and makes it possible to realize TI phase in conventional semiconductor 2DEG using the well-developed semiconductor fabrication techniques [47–49]. The presence of the TI phase in PQWs with antidot lattice can largely advance the application of this new quantum state in existing electronics and optoelectronics devices. The general designing principle proposed in this work, i.e., the gauge field acting on slow orbital motion induced by interband coupling, paves a new way for generating nontrivial topological phases, such as quantum spin Hall phase and even quantum anomalous Hall phases by doping magnetic ions, in conventional semiconductor 2DEGs, and suggests a promising approach to integrate it in well developed semiconductor electronic devices.

V. ACKNOWLEDGMENTS

This work was supported by the NSFC Grants Nos. 11434010, 11304306 and the grant No. 2011CB922204 from the MOST of China. KC would like to appreciate Prof. S. C. Zhang for helpful discussions. LKS and WKL contributed equally to this work.

VI. APPENDIX A: EFFECTIVE GAUGE FIELD IN SPIN-ORBIT COUPLED SYSTEMS

In the spin-orbit coupled system, adopting the Born-Oppenheimer approximation, the total Hamiltonian can be divided into two parts:

$$\hat{H}(\hat{\mathbf{k}}, \hat{\mathbf{r}}, \hat{\sigma}) = \hat{H}_{\text{orb}}(\hat{\mathbf{k}}, \hat{\mathbf{r}}) + H_{\text{s-o}}(\hat{\mathbf{k}}, \hat{\sigma}),$$

where $\hat{H}_{\text{orb}}(\hat{\mathbf{k}}, \hat{\mathbf{r}})$ stands for the intra-band (slow) orbital motion part, and $H_{\text{s-o}}(\hat{\mathbf{k}}, \hat{\sigma})$ is the inter-band (fast) spin-orbit part. For a given eigenvalue \mathbf{k} of the momentum

operator $\hat{\mathbf{k}}$, the eigenstates of the spin-orbit part is denoted by $|n(\mathbf{k})\rangle$ ($n = 1, 2, \dots$) and the corresponding eigenenergies are $\epsilon_n(\mathbf{k})$. We work in the momentum representation of the orbital part and expand the eigenstate of $\hat{H}(\hat{\mathbf{k}}, \hat{\mathbf{r}}, \hat{\sigma})$ in this representation, $|\Psi(\mathbf{k})\rangle \equiv |\mathbf{k}|\Psi\rangle$, as

$$|\Psi(\mathbf{k})\rangle = \sum_{n, \mathbf{k}} \phi_n(\mathbf{k}) |\chi_n(\mathbf{k})\rangle.$$

In the momentum representation, we have $\hat{\mathbf{r}} = i\nabla_{\mathbf{k}}$ and $\hat{\mathbf{k}} = \mathbf{k}$. Substituting into $\hat{H}(\mathbf{k}, \hat{\mathbf{r}}, \hat{\sigma})|\Psi(\mathbf{k})\rangle = E|\Psi(\mathbf{k})\rangle$, we have

$$\sum_n H_{m,n}(\mathbf{k}) \phi_n(\mathbf{k}) = E \phi_m(\mathbf{k}),$$

where

$$\begin{aligned} H_{m,n}(\mathbf{k}) &\equiv \delta_{m,n} \epsilon_m(\mathbf{k}) + \langle \chi_m(\mathbf{k}) | \hat{H}_{\text{orb}}(\mathbf{k}, \hat{\mathbf{r}}) | \chi_n(\mathbf{k}) \rangle \\ &= \delta_{m,n} \epsilon_m(\mathbf{k}) + \hat{H}_{\text{orb}}(\mathbf{k}, \hat{\mathbf{r}} - \mathbf{A}_{m,n}(\mathbf{k})) \end{aligned}$$

contains a pure gauge $\mathbf{A}_{m,n}(\mathbf{k}) \equiv -i \langle \chi_m(\mathbf{k}) | \nabla_{\mathbf{k}} | \chi_n(\mathbf{k}) \rangle$. By now the above equation is still exact. Now we make the Born-Oppenheimer approximation and consider adiabatic transport, i.e., neglect the off-diagonal coupling between different spin-orbit energy bands, to arrive at the single-band description

$$H_n(\mathbf{k}, \hat{\mathbf{r}}'_n) \phi_n(\mathbf{k}) = E \phi_n(\mathbf{k}),$$

where the effective single-band Hamiltonian on the orbital motion

$$H_n(\mathbf{k}, \hat{\mathbf{r}}'_n) = \epsilon_n(\mathbf{k}) + \hat{H}_{\text{orb}}(\mathbf{k}, \hat{\mathbf{r}}'_n),$$

where $\hat{\mathbf{r}}'_n = \hat{\mathbf{r}} - \mathbf{A}_n(\mathbf{k})$ contains an effective gauge field for the slow orbital motion:

$$\mathbf{A}_n(\mathbf{k}) = -i \langle \chi_n(\mathbf{k}) | \nabla_{\mathbf{k}} | \chi_n(\mathbf{k}) \rangle.$$

Specifically, for the BHZ model of 2D TIs in the presence of an in-plane uniform electric field, the slow orbital part is

$$\hat{H}_{\text{orb}}(\hat{\mathbf{k}}, \hat{\mathbf{r}}) = C - Dk^2 - e\mathbf{E} \cdot \mathbf{r},$$

and the fast spin-orbital part $H_{\text{s-o}}(\hat{\mathbf{k}}, \hat{\sigma})$ is

$$\begin{pmatrix} M - Bk^2 & Ak_+ & 0 & 0 \\ Ak_- & -M + Bk^2 & 0 & 0 \\ 0 & 0 & M - Bk^2 & Ak_- \\ 0 & 0 & Ak_+ & -M + Bk^2 \end{pmatrix},$$

and

$$A_{x,n} = s_n \frac{k_y}{2k^2} \left[1 + t_n \frac{Bk^2 - M}{[A^2k^2 + (M - Bk^2)^2]^{1/2}} \right],$$

$$A_{y,n} = s_n \frac{k_x}{2k^2} \left[1 + t_n \frac{Bk^2 - M}{[A^2k^2 + (M - Bk^2)^2]^{1/2}} \right].$$

where $s_n = \pm 1$ for spin-up/down block, and $t_n = \pm 1$ for the electron in conduction/valence band ($n = 1, 2, 3, 4$). The effective vector potential leads to the non-trivial effective gauge field with the strength

$$F_{xy,n}(\mathbf{k}) \equiv i[x', y'] = i[\partial_{k_x} - A_x, \partial_{k_y} - A_y] \\ = (\nabla_{\mathbf{k}} \times \mathbf{A})_z = \lambda_n \frac{A^2(M + Bk^2)}{2[A^2k^2 + (M - Bk^2)^2]^{3/2}},$$

where $\lambda_n = s_n \times t_n = \pm 1$ ($n = 1, 2, 3, 4$). Within the Born-Oppenheimer approximation, the equation of motion for the n -th band can be written as

$$\dot{x}'_n = \frac{\partial H_n}{\hbar \partial k_x} + F_{xy,n}(k) \dot{k}_y, \\ \dot{y}'_n = \frac{\partial H_n}{\hbar \partial k_y} - F_{xy,n}(k) \dot{k}_x, \\ \dot{k}_i = eE_i/\hbar,$$

we can see that the gauge field strength $F_{xy,n} = (\nabla_{\mathbf{k}} \times \mathbf{A})_z$ acts as a Lorentz force in the k -space, acting on spin-up and spin-down electrons in opposite directions, which is perpendicular to electron momentum.

VII. APPENDIX B: EFFECTIVE SPIN-ORBIT COUPLING IN A QUANTUM WELL

For a symmetric QW grown along (001) direction (the z axis), effective spin-orbit coupling exists between subbands with opposite parities. This effective spin-orbit coupling comes from interband coupling and can be understood by reducing the 8×8 Kane Hamiltonian to a 2×2 effective Hamiltonian [50].

To the first order of k , the 8×8 Kane Hamiltonian in the basis ($i|S, \uparrow\rangle, i|S, \downarrow\rangle, |3/2, 1/2\rangle, |3/2, -1/2\rangle, |3/2, 3/2\rangle, |3/2, -3/2\rangle, |1/2, 1/2\rangle, |1/2, -1/2\rangle$) around the Γ point is

$$H_{8 \times 8} = \begin{pmatrix} H_c & H_{cv} \\ H_{cv}^\dagger & H_v \end{pmatrix},$$

where $H_c = \epsilon_c I_{2 \times 2}$ and $H_v = \epsilon_v I_{4 \times 4} \oplus \epsilon_s I_{2 \times 2}$ are 2×2 and 6×6 diagonal part for conduction and valence bands, and the 2×6 matrix

$$H_{cv} = \begin{pmatrix} \frac{-\sqrt{2}Pk_z}{\sqrt{6}} & \frac{-Pk_-}{\sqrt{6}} & \frac{Pk_+}{\sqrt{2}} & 0 & \frac{Pk_z}{\sqrt{3}} & \frac{-Pk_-}{\sqrt{3}} \\ \frac{Pk_+}{\sqrt{6}} & -\frac{\sqrt{2}Pk_z}{\sqrt{3}} & 0 & \frac{Pk_-}{\sqrt{2}} & \frac{Pk_+}{\sqrt{3}} & \frac{Pk_z}{\sqrt{3}} \end{pmatrix}$$

represents the interband coupling. Specifically, $\epsilon_i = \hbar^2 k^2/(2m) + V_i$ is the kinetic energy plus the total potential for the conduction/valence/spin-split ($i = c/v/s$) bands, with $V_c - V_v = E_g$ the band gap and $V_v - V_s = \Delta_0$ the band off set. $k_\pm = k_x \pm ik_y$ and $P = -i(\hbar/m_0) \langle S_c | p_x | X_v \rangle$ parameterize the interband coupling.

The eigenvalue problem can be expressed as

$$\begin{pmatrix} H_c & H_{cv} \\ H_{cv}^\dagger & H_v \end{pmatrix} \begin{pmatrix} \varphi_c \\ \varphi_v \end{pmatrix} = \varepsilon \begin{pmatrix} \varphi_c \\ \varphi_v \end{pmatrix},$$

where φ_c is a two-component spinor for conduction bands and φ_v is a six-component spinor for valence bands. Since we focus on the conduction bands, $\varphi_v = (\varepsilon - H_v)^{-1} H_{cv}^\dagger \varphi_c$ can be eliminated and gives the effective Schrödinger-type equation $H_{\text{eff}} \varphi_c = \varepsilon \varphi_c$, with $H_{\text{eff}} = H_c + H_{cv} (\varepsilon - H_v)^{-1} H_{cv}^\dagger$ for conduction bands. Without loss of generality, we assume the QW is non-uniform only along the z direction, e.g., a PQW. By straightforward algebra, we have $H_{\text{eff}}^{\uparrow\downarrow} = (H_{\text{eff}}^{\uparrow\downarrow})^\dagger = \sum_{i=v,s} (k_-/3) P(z) [(\varepsilon - \epsilon_i(z))^{-1} P(z), k_z]$, where $H_{\text{eff}}^{\uparrow\downarrow}$ and $H_{\text{eff}}^{\downarrow\uparrow}$ represent the effective spin-orbit coupling between the spin up and down electron.

Since we focus on the lowest conduction subbands, we have $\varepsilon - \epsilon_v(z) \approx E_g(z)$ and $\varepsilon - \epsilon_s(z) \approx E_g(z) + \Delta_0(z) \equiv E_{g'}(z)$. Because $E_g(z)$ and $E_{g'}(z)$ are much larger than the subband energies in the wide QWs under consideration, we keep the zero-th order terms $E_g^{-1}(z)$ and $E_{g'}(z)^{-1}$ in the expansion, and project the spin-orbit coupling operator $H_{\text{eff}}^{\uparrow\downarrow}$ into the two lowest spin-degenerate subbands ($|\chi_1(z)\rangle, |\chi_2(z)\rangle$) to obtain the ISOI $\eta \tau_x (k_x \sigma^x + k_y \sigma^y)$, where η is given in Eq. (4), σ^i denotes the real electron spin, and τ_i refers to the Pauli matrix describing the subband index.

VIII. APPENDIX C: BAND EDGE WAVE FUNCTIONS IN FOLDED BRILLOUIN ZONE

We consider a PQW in the presence of an antidot lattice, which can be generally described by a potential $V(\mathbf{r}) = \sum_{\mathbf{q}} \tilde{V}(\mathbf{q}) e^{i\mathbf{q} \cdot \mathbf{r}}$ with the lattice periodicity.

For a triangular antidot lattice, the reciprocal lattice vectors in the hexagonal Brillouin zone are $\mathbf{Q}_1 = (2\pi/3a)(3, 0)$, $\mathbf{Q}_2 = (2\pi/3a)(-3/2, -3\sqrt{3}/2)$, $\mathbf{Q}_3 = -(\mathbf{Q}_1 + \mathbf{Q}_2)$. The envelope functions of the lowest miniband at the band edge ($k = 0$, Γ point) is $u_{\Gamma,1}(\mathbf{r}) = 1 - \sum_{l=1}^3 [2m\tilde{V}(\mathbf{Q}_l)/\hbar^2 Q^2] \cos(\mathbf{Q}_l \cdot \mathbf{r})$. For higher minibands, their envelope functions $u_{\Gamma,n}(\mathbf{r})$ ($n = 2, 3, 4, 5, 6, 7$) at the band edge are linear combinations of the six wave vector components ($e^{\pm i\mathbf{Q}_1 \cdot \mathbf{r}}, e^{\pm i\mathbf{Q}_2 \cdot \mathbf{r}}, e^{\pm i\mathbf{Q}_3 \cdot \mathbf{r}}$), e.g., $u_{\Gamma,2}(\mathbf{r}) \propto \sum_{l=1}^3 \sin(\mathbf{Q}_l \cdot \mathbf{r})$ and $u_{\Gamma,7}(\mathbf{r}) \propto \sum_{l=1}^3 \cos(\mathbf{Q}_l \cdot \mathbf{r})$. The most important minibands are $u_{k,1}(r)$, $u_{k,2}(r)$ and $u_{k,4}(r)$: the lowest nontrivial minigap occurs between $u_{k,1}(r)$ and $u_{k,2}(r)$, and the second nontrivial minigap occurs between $u_{k,2}(r)$ and $u_{k,4}(r)$.

IX. APPENDIX D: EFFECTIVE BHZ HAMILTONIAN NEAR THE Γ POINT

The lowest two subbands $\chi_1(z)$ and $\chi_2(z)$ in a PQW have even and odd opposite parities, an effective spin-orbit interaction $\langle \chi_1(z) | \eta(z) (k_x \sigma^x + k_y \sigma^y) | \chi_2(z) \rangle$ appears. When the Brillouin zone is folded by the triangular anti-dot lattice, the lowest nontrivial minigap appears between the miniband pair $|\chi_1(z), u_{k,2}(r)\rangle$ and

$|\chi_2(z), u_{k,1}(r)\rangle$, i.e., the second miniband of the first subband and the first miniband of the second subband. The second nontrivial minigap appears between the miniband pair $|\chi_2(z), u_{k,2}(r)\rangle$ and $|\chi_1(z), u_{k,4}(r)\rangle$, i.e., the second miniband of the second subband and the fourth miniband of the first subband. To obtain an effective Hamiltonian near each minigap, we project the Hamiltonian $H = \hbar^2 k^2/2m + \Delta_{12}\tau_z + \eta\tau_x(k_x\sigma^x + k_y\sigma^y) + V(x, y)$ onto the corresponding miniband pair and obtain an effective BHZ model Eq. (5) in the basis $|\psi_+, \uparrow\rangle, |\psi_-, \downarrow\rangle, |\psi_+, \downarrow\rangle, |\psi_-, \uparrow\rangle$, where $|\psi_+\rangle$ is the miniband above $|\psi_-\rangle$ by $2M$ at the Γ point, $B = -\hbar^2/2m^*$ characterizes the band dispersions with the effective mass m^* near the band edge, and A characterizes the intersubband spin-orbit coupling. At the Γ point

$$\begin{aligned} & \langle \psi_+ | \eta(z)(k_x\sigma^x + k_y\sigma^y) | \psi_- \rangle \\ &= \langle \chi_{1(2)}(z) | \eta(z) | \chi_{2(1)}(z) \rangle \\ & \cdot \langle u_{k,2(2)}(r) | (-i\partial_x\sigma_x - i\partial_y\sigma_y) | u_{k,1(4)}(r) \rangle \\ &= A(k_x\sigma^x + k_y\sigma^y). \end{aligned}$$

The accurate coupling strength can be estimated by numerical calculating based on the eight-band Kane model.

For BHZ model, a Z_2 topological transition from the normal phase to the topological insulator phase would occur when $M = \Delta_{12} - \Delta_{\text{Fold}}$ [see Fig. 1(b)] changes sign from positive to negative, which can be controlled by adjusting the lattice constants and etching depths of antidots.

X. APPENDIX E: THE EFFECTIVE HAMILTONIAN REDUCED NUMERICALLY FROM THE EIGHT-BAND KANE MODEL

At the Γ point, the wave functions in the eight-band $\mathbf{k} \cdot \mathbf{p}$ Hamiltonian are

$$\psi_m = \begin{pmatrix} F_1^{(m)}(z) \\ F_2^{(m)}(z) \\ F_3^{(m)}(z) \\ F_4^{(m)}(z) \\ \vdots \\ F_8^{(m)}(z) \end{pmatrix} e^{i\mathbf{k}_{\parallel} \cdot \tilde{\mathbf{r}}},$$

which can be obtained by solving the secular equation $H_{8 \times 8}^{(0)} \psi_m = E_m \psi_m$.

Considering the two lowest electron subbands, we obtain the effective two-dimensional Hamiltonian by averaging the z component in the Hamiltonian

$$H_{\text{eff}}(\mathbf{k}_{\parallel}) = \langle \Psi(z) | H | \Psi(z) \rangle,$$

where the matrix element of the Hamiltonian is

$$\begin{aligned} \langle H_{\text{eff}} \rangle_{mn} &= \langle \psi^{(m)} | H_{8 \times 8} | \psi^{(n)} \rangle \\ &= \sum_{i,j=1}^8 \langle F_i^{(m)}(z) | H_{ij} | F_j^{(n)}(z) \rangle. \end{aligned}$$

The Hamiltonian can be divided into

$$\begin{aligned} H &= H^{(0)} + H', \\ H'(\mathbf{q}, \hat{k}_z) &= \alpha(\mathbf{q}) + \beta(\mathbf{q}) \hat{k}_z + \gamma(\mathbf{q}) \hat{k}_z^2. \end{aligned}$$

Then we have

$$\begin{aligned} \langle H_{\text{eff}} \rangle_{mn} &= E_m \delta_{m,n} + \sum_{i,j=1}^8 \langle F_i^{(m)}(z) | [\alpha(\mathbf{q})]_{ij} | F_j^{(n)}(z) \rangle \\ &+ \langle F_i^{(m)}(z) | [\beta(\mathbf{q})]_{ij} \hat{k}_z | F_j^{(n)}(z) \rangle \\ &+ \langle F_i^{(m)}(z) | [\gamma(\mathbf{q})]_{ij} \hat{k}_z^2 | F_j^{(n)}(z) \rangle. \end{aligned}$$

The contribution of the subbands other than the two lowest electron subbands should also be considered in the reducing process, which can be done by using Löwdin perturbation theory. We include the lowest 20 electron subbands and 54 highest hole subbands in the QW respectively and divide them into the weakly coupled subsets S_1 and S_2 . The set S_1 includes the two lowest electron subbands $|\chi_1\rangle$ and $|\chi_2\rangle$, the other subbands are included in the set S_2 . The Hamiltonian is reduced into set S_1 using the Löwdin perturbation method,

$$H_{mm'}^{(2)} = \frac{1}{2} \sum_l H'_{ml} H'_{lm'} \left[\frac{1}{E_m - E_l} + \frac{1}{E_{m'} - E_l} \right],$$

where the indices m correspond to states in the set A , the indices l correspond to states in the set B , and

$$H'_{ml} = \langle \psi_m | H' | \psi_l \rangle.$$

Finally we obtain the effective two-dimensional Hamiltonian $H_{\text{eff}}^{4 \times 4}$ in the basis $|\chi_1, \uparrow\rangle, |\chi_2, \downarrow\rangle, |\chi_1, \downarrow\rangle, |\chi_2, \uparrow\rangle$:

$$\begin{pmatrix} E_1 + B_1 \cdot k_{\parallel}^2 & Ak_+ & 0 & 0 \\ Ak_- & E_2 + B_2 \cdot k_{\parallel}^2 & 0 & 0 \\ 0 & 0 & E_1 + B_1 \cdot k_{\parallel}^2 & Ak_- \\ 0 & 0 & Ak_+ & E_2 + B_2 \cdot k_{\parallel}^2 \end{pmatrix},$$

where

$$\begin{aligned} E_1 &= 0.05351 \text{ eV}, \\ B_1 &= 0.86571 \text{ eV} \cdot \text{nm}^2, \\ E_2 &= 0.14396 \text{ eV}, \\ B_2 &= 0.67969 \text{ eV} \cdot \text{nm}^2, \\ A &= 0.01041 \text{ eV} \cdot \text{nm}. \end{aligned}$$

In order to examine the validity of the 4-band Hamiltonian, we plot the band structure of the GaAs/In_xGa_{1-x}As/GaAs PQW calculated by the 4-band model and compare it with the eight-band $\mathbf{k} \cdot \mathbf{p}$ model (see Fig. 2a in the manuscript). One can see clearly that the band structure obtained from the 4-band model [the solid lines in Fig. 2a] is in good agreement with that obtained from the eight-band model [the dashed lines in Fig. 2a].

XI. APPENDIX F: VERIFICATION OF NON-TRIVIAL Z_2 TOPOLOGICAL INVARIANT

Topological insulators with dissipationless edge states and ordinary insulators are distinguished by different Z_2 invariants. For 2D systems, Fu and Kane [11] have shown that the Z_2 invariant can be determined from the parity of the occupied band at the four time-reversal invariant momenta in the Brillouin zone. The Z_2 invariant $\nu = 0, 1$, which distinguishes the quantum spin-Hall phase in two dimensions, is given by

$$(-1)^\nu = \prod_i \delta_i, \\ \delta_i = \prod_{m=1}^N \xi_{2m}(\Gamma_i),$$

where $\xi_{2m}(\Gamma_i) = \pm 1$ is the parity eigenvalue of the $2m$ th occupied energy band at the time-reversal invariant point Γ_i , which shares the same eigenvalue $\xi_{2m} = \xi_{2m-1}$ with its Kramer degenerate partner. The four time-reversal invariant points $\Gamma_{i=(n_1 n_2)} = (n_1 \mathbf{Q}_1 + n_2 \mathbf{Q}_2)/2$, where $n_1, n_2 = 0, 1$. The calculated parity eigenvalue of the $2m$ th ($m = 1, 2, 3, 4, 5, 6$) occupied energy band at Γ_i are listed:

m	$\xi_{2m}(\Gamma_{00})$	$\xi_{2m}(\Gamma_{01})$	$\xi_{2m}(\Gamma_{10})$	$\xi_{2m}(\Gamma_{11})$
1	+	-	-	-
2	+	+	+	+
3	-	-	-	-
4	+	+	+	+
5	+	+	+	+
6	-	-	-	-

From the above calculation, we can confirm that the Z_2 invariant $\nu = 1$ at the $2m$ th ($m = 2, 5, 6$) occupied band where the minigaps open, and the system enters the TI phase and the dissipationless edge states appear.

-
- [1] D. J. Thouless, M. Kohmoto, M. P. Nightingale, and M. den Nijs, *Quantized Hall Conductance in a Two-Dimensional Periodic Potential*, Phys. Rev. Lett. **49**, 405 (1982).
 - [2] Q. Niu, D. J. Thouless, and Y. S. Wu, *Quantized Hall conductance as a topological invariant*, Phys. Rev. B **31** 3372 (1985).
 - [3] F. D. M. Haldane, *Model for a Quantum Hall Effect without Landau Levels: Condensed-Matter Realization of the "Parity Anomaly"*, Phys. Rev. Lett. **61**, 2015 (1988).
 - [4] M. Z. Hasan and C. L. Kane, *Colloquium: Topological insulators*, Rev. Mod. Phys. **82**, 3045 (2010).
 - [5] X. L. Qi and S. C. Zhang, *Topological insulators and superconductors*, Rev. Mod. Phys. **83**, 1057 (2011).
 - [6] C. L. Kane and E. J. Mele, *Z_2 Topological Order and the Quantum Spin Hall Effect*, Phys. Rev. Lett. **95**, 146802 (2005).
 - [7] B. A. Bernevig, T. L. Hughes, and S. C. Zhang, *Quantum Spin Hall Effect and Topological Phase Transition in HgTe Quantum Wells*, Science **314**, 1757 (2006).
 - [8] M. König, S. Wiedmann, C. Brüne, A. Roth, H. Buhmann, L. W. Molenkamp, X. L. Qi, S. C. Zhang, *Quantum Spin Hall Insulator State in HgTe Quantum Wells*, Science **318**, 766 (2007).
 - [9] I. Knez, R. R. Du, and G. Sullivan, *Evidence for Helical Edge Modes in Inverted InAs/GaSb Quantum Wells*, Phys. Rev. Lett. **107**, 136603 (2011).
 - [10] L. Fu, C. L. Kane, and E. J. Mele, *Topological Insulators in Three Dimensions*, Phys. Rev. Lett. **98**, 106803 (2007);
 - [11] L. Fu and C. L. Kane, *Topological insulators with inversion symmetry*, Phys. Rev. B **76**, 045302 (2007).
 - [12] D. Hsieh, D. Qian, L. Wray, Y. Xia, Y. S. Hor, R. J. Cava, and M. Z. Hasan, *A topological Dirac insulator in a quantum spin Hall phase*, Nature **452**, 970 (2008).
 - [13] Y. L. Chen, J. G. Analytis, J.-H. Chu, Z. K. Liu, S.-K. Mo, X. L. Qi, H. J. Zhang, D. H. Lu, X. Dai, Z. Fang, S. C. Zhang, I. R. Fisher, Z. Hussain, and Z.-X. Shen, *Experimental Realization of a Three-Dimensional Topological Insulator, Bi₂Te₃*, Science **325**, 178 (2009).
 - [14] Y. Xia, D. Qian, D. Hsieh, L. Wray, A. Pal, H. Lin, A. Bansil, D. Grauer, Y. S. Hor, R. J. Cava, and M. Z. Hasan, *Observation of a large-gap topological-insulator class with a single Dirac cone on the surface*, Nature Phys. **5**, 398 (2009).
 - [15] H. Lin, L. A. Wray, Y. Xia, S. Xu, S. Jia, R. J. Cava, A. Bansil, and M. Z. Hasan, *Half-Heusler ternary compounds as new multifunctional experimental platforms for topological quantum phenomena*, Nature Mater. **9**, 546 (2010).
 - [16] M. Franz, *Topological insulators: Starting a new family*, Nature Materials **9**, 536 (2010).
 - [17] K. Yang, W. Setyawan, S. Wang, M. B. Nardelli, and S. Curtarolo, *A search model for topological insulators with high-throughput robustness descriptors*, Nature Mater. **11**, 614 (2012).
 - [18] S. Chadov, X. L. Qi, Jürgen Kübler, G. H. Fecher, C. Felser, and S. C. Zhang, *Tunable multifunctional topological insulators in ternary Heusler compounds*, Nature Mater. **9**, 541 (2010).
 - [19] D. Xiao, Y. Yao, W. Feng, J. Wen, W. Zhu, X. Q. Chen, G. M. Stocks, and Z. Zhang, *Half-Heusler Compounds as a New Class of Three-Dimensional Topological Insu-*

- lators, Phys. Rev. Lett. **105**, 096404 (2010).
- [20] O. P. Sushkov and A. H. Castro Neto, *Topological Insulating States in Laterally Patterned Ordinary Semiconductors*, Phys. Rev. Lett. **110**, 186601 (2013).
- [21] D. Xiao, W. G. Zhu, Y. Ran, N. Nagaosa, and S. Okamoto, *Interface engineering of quantum Hall effects in digital transition metal oxide heterostructures*, Nature Commun. **2**, 596 (2011).
- [22] Y. Xu, B. H. Yan, H. J. Zhang, J. Wang, G. Xu, P. Z. Tang, W. H. Duan, and S. C. Zhang, *Large-Gap Quantum Spin Hall Insulators in Tin Films*, Phys. Rev. Lett. **111**, 136804 (2013).
- [23] J. Li and K. Chang, *Electric field driven quantum phase transition between band insulator and topological insulator*, Appl. Phys. Lett. **95**, 222110 (2009).
- [24] M. S. Miao, Q. Yan, C. G. Van de Walle, W. K. Lou, L. L. Li, and K. Chang, *Polarization-Driven Topological Insulator Transition in a GaN/InN/GaN Quantum Well*, Phys. Rev. Lett. **109**, 186803 (2012).
- [25] D. Zhang, W. K. Lou, M. S. Miao, S. C. Zhang, and K. Chang, *Interface-Induced Topological Insulator Transition in GaAs/Ge/GaAs Quantum Wells*, Phys. Rev. Lett. **111**, 156402 (2013).
- [26] J. Hu, J. Alicea, R. Q. Wu, and M. Franz, *Giant Topological Insulator Gap in Graphene with 5d Adatoms*, Phys. Rev. Lett. **109**, 266801 (2012).
- [27] M. I. Katsnelson, F. Guinea, and M. A. H. Vozmediano, *In-plane magnetic textures at the surface of topological insulators*, EUROPHYS LETT **104**, 17001 (2013).
- [28] F. Wilczek and A. Zee, *Appearance of Gauge Structure in Simple Dynamical Systems*, Phys. Rev. Lett. **52**, 2111 (1984).
- [29] C. P. Sun and M. L. Ge, *Generalizing Born-Oppenheimer approximations and observable effects of an induced gauge field*, Phys. Rev. D **41**, 1349 (1990).
- [30] J. E. Moore and L. Balents, *Topological invariants of time-reversal-invariant band structures*, Phys. Rev. B **75**, 121306(R) (2007).
- [31] N. H. Lindner, G. Refael and V. Galitski, *Floquet topological insulator in semiconductor quantum wells*, Nature Phys. **7**, 490 (2011).
- [32] D. Weiss, M. L. Roukes, A. Menschig, P. Grambow, K. von Klitzing, G. Weimann, *Electron pinball and commensurate orbits in a periodic array of scatterers*, Phys. Rev. Lett., **66**, 2790 (1991).
- [33] J. Eroms, M. Zitzlsperger, D. Weiss, J. H. Smet, C. Albrecht, R. Fleischmann, M. Behet, J. DeBoeck, G. Borghs, *Skipping orbits and enhanced resistivity in large-diameter InAs/GaSb antidot lattices*, Phys. Rev. B **59**, 7829(R) (1999).
- [34] C. Albrecht, J. H. Smet, D. Weiss, K. von Klitzing, R. Hennig, M. Langenbuch, M. Suhrke, U. Rössler, V. Umansky, H. Schweizer, *Fermiology of Two-Dimensional Lateral Superlattices*, Phys. Rev. Lett. **83**, 2234 (1999).
- [35] C. Albrecht, J. H. Smet, K. von Klitzing, D. Weiss, V. Umansky, H. Schweizer, *Evidence of Hofstadter's Fractal Energy Spectrum in the Quantized Hall Conductance*, Phys. Rev. Lett. **86**, 147 (2001).
- [36] K. Bittkau, Ch. Menk, Ch. Heyn, D. Heitmann, and C. M. Hu, *Far-infrared photoconductivity of electrons in an array of nanostructured antidots*, Phys. Rev. B **68**, 195303 (2003).
- [37] Z. Q. Yuan, C. L. Yang, R. R. Du, L. N. Pfeiffer, and K. W. West, *Microwave photoresistance of a high-mobility two-dimensional electron gas in a triangular antidot lattice*, Phys. Rev. B **74**, 075313 (2006).
- [38] C. H. Park and S. G. Louie, *Making Massless Dirac Fermions from a Patterned Two-dimensional Electron Gas*, Nano Lett. **9**, 1793 (2009).
- [39] S. Wang, L. Z. Tan, W. Wang, S. G. Louie, and N. Lin, *Manipulation and Characterization of Aperiodical Graphene Structures Created in a Two-Dimensional Electron Gas*, Phys. Rev. Lett. **113**, 196803 (2014).
- [40] A. Sacedón, F. González-Sanz, E. Calleja, E. Muñoz, S. I. Molina, F. J. Pacheco, D. Araújo, R. García, M. Lourenço, Z. Yang, P. Kidd, and D. Dunstan, *Design of InGaAs linear graded buffer structures*, Appl. Phys. Lett. **66**, 3334 (1995).
- [41] J. Liang, Y. C. Chua, M. O. Manasreh, E. Marega, Jr., and G. J. Salamo, *Broad-band photoresponse from InAs quantum dots embedded into InGaAs graded well*, IEEE Electron Device Letters **26**, 631 (2005).
- [42] N. Dai, G. A. Khodaparast, F. Brown, R. E. Doezema, S. J. Chung, and M. B. Santos, *Band offset determination in the strained-layer InSb/Al_xIn_{1-x}Sb system*, Appl. Phys. Lett. **76**, 3905 (2000).
- [43] K. Lai, W. Kundhikanjana, M. A. Kelly, Z. X. Shen, J. Shabani, and M. Shayegan, *Imaging of Coulomb-Driven Quantum Hall Edge States*, Phys. Rev. Lett. **107**, 176809 (2011).
- [44] J. A. Sobota, S.-L. Yang, A. F. Kemper, J. J. Lee, F. T. Schmitt, W. Li, R. G. Moore, J. G. Analytis, I. R. Fisher, P. S. Kirchmann, T. P. Devereaux, and Z. X. Shen, *Direct Optical Coupling to an Unoccupied Dirac Surface State in the Topological Insulator Bi₂Se₃*, Phys. Rev. Lett. **111**, 136802 (2013).
- [45] Y. Ueda, A. Furuta, H. Okuda, M. Nakatake, H. Sato, H. Namatame, M. Taniguchi, *Photoemission and inverse-photoemission studies of Bi₂Y₃ (Y=S, Se, Te) semiconductors*, J. Electron Spectrosc. Relat. Phenom. **101**, 677 (1999).
- [46] D. Niesner, Th. Fauster, S. V. Eremeev, T. V. Menshchikova, Yu. M. Koroteev, A. P. Protopogov, E. V. Chulkov, O. E. Tereshchenko, K. A. Kokh, O. Alekperov, A. Nadjafov, and N. Mamedov, *Unoccupied topological states on bismuth chalcogenides*, Phys. Rev. B **86**, 205403 (2012).
- [47] W. D. Rice, J. Kono, S. Zybelle, S. Winnerl, J. Bhattacharyya, H. Schneider, M. Helm, B. Ewers, A. Chernikov, M. Koch, S. Chatterjee, G. Khitrova, H. M. Gibbs, L. Schneebeli, B. Breddermann, M. Kira, and S. W. Koch, *Observation of Forbidden Exciton Transitions Mediated by Coulomb Interactions in Photoexcited Semiconductor Quantum Wells*, Phys. Rev. Lett **110**, 137404 (2013).
- [48] T. R. Merritt, M. A. Meeker, B. A. Magill, G. A. Khodaparast, S. McGill, J. G. Tischler, S. G. Choi, and C. J. Palmstrom, *Photoluminescence lineshape and dynamics of localized excitonic transitions in InAsP epitaxial layers*, J. Appl. Phys. **115**, 193503 (2014).
- [49] Y. Zhang, and J. J. Heremans, *Effects of ferromagnetic nanopillars on spin coherence in an InGaAs quantum well*, Solid State Commun. **177**, 36 (2014).
- [50] P. O. Löwdin, *A Note on the Quantum-Mechanical Perturbation Theory*, J. Chem. Phys. **19**, 1396 (1951).